

Enhanced molecular diffusion near a soft fluctuating membrane

Ali Mohammadi,¹ Zhen Li,¹ Sophie Marbach,² and Micheline Abbas³

¹*Department of Mechanical Engineering, Clemson University, Clemson, SC 29634, USA*

²*CNRS, Sorbonne Université, Physicochimie des Electrolytes et Nanosystèmes Interfaciaux, F-75005 Paris, France*

³*Laboratoire de Génie Chimique, Université de Toulouse, CNRS, INPT, UPS, Toulouse, France*

(*Electronic mail: micheline.abbas@toulouse-inp.fr)

(*Electronic mail: sophie.marbach@cnrs.fr)

(Dated: 8 July 2025)

Particles diffusing near interfaces face anisotropic resistance to motion due to hydrodynamic interactions. While this has been extensively studied near *hard* interfaces since the works of Lorentz and Brenner, our understanding of diffusion near *soft, thermally fluctuating* interfaces remains limited. Previous studies have predominantly focused on particles much larger than the molecular scale at which thermal fluctuations become important. In this work, we numerically investigate the dynamics of individual solvent molecules near a thermally fluctuating lipid membrane, a canonical soft interface in biology. We observe that diffusive motion of solvent molecules near the fluctuating membrane is slightly enhanced compared to a flat rigid interface and significantly more so than near an undulated rigid interface. This enhancement in diffusive motion of solvent molecules arises from spontaneous momentum exchanges between the moving membrane and adjacent molecules, promoting mixing. Notably, this dispersion effect overcomes geometric trapping that slows diffusion near the rigid undulated interface. Our analysis reveals that the momentum transfer near the fluctuating membrane is so efficient that it resembles an effective slip boundary condition over a length scale equal to the fluctuation height. These molecular-scale mechanisms differ from those of larger particles, where hydrodynamic memory and elasticity effects can be at play as they relax over timescales comparable to significant diffusive motion. Our findings advance understanding of enhanced diffusive motion and promoted mixing near soft fluctuating membranes involved in diverse biological processes and soft-matter technologies containing natural and model cell membranes.

I. INTRODUCTION

The diffusion of dispersed species near interfaces plays a critical role in many interfacial phenomena such as adsorption and capture. In biological systems, for instance, the interplay between diffusion and intermittent adsorption strongly influences protein binding rates to cells and other targets^{1,2}. Similar competition between diffusive transport and physicochemical interactions is also relevant in technological applications, including surface-based detection sensors³ and film formation processes in coatings⁴. In an unbounded viscous fluid, the diffusion of dilute particles is characterized by their self-diffusion coefficient D_b . Einstein's relation connects D_b to a friction coefficient γ , as $D_b = k_B T / \gamma$ with $k_B T$ representing thermal energy. For a spherical particle of radius a substantially larger than fluid molecules, freely moving in an unbounded fluid at low Reynolds numbers, the friction coefficient in a fluid with dynamic viscosity η is given by Stokes' law⁵, $\gamma = 6\pi\eta a$, giving the Stokes-Einstein relation $D_b = k_B T / 6\pi\eta a$.

In the presence of an interface, hydrodynamic interactions between the particle and the interface increase the friction coefficient γ , and thus decrease diffusion. Several analytical expressions have been obtained near *hard, flat* interfaces. Lorentz obtained pioneering expressions for the diffusion of a spherical particle moving near a rigid wall⁶, using a method of im-

ages with a first-order reflection. When the particle's radius a is much smaller than its instantaneous distance z from the wall, $a/z \ll 1$, the local diffusion coefficients may be approximated by

$$\frac{D_{\perp}(z)}{D_b} \approx 1 + \frac{9}{8} \frac{a}{z} \quad \text{and} \quad \frac{D_{\parallel}(z)}{D_b} \approx 1 + \frac{9}{16} \frac{a}{z} \quad (1)$$

for the perpendicular and parallel directions with respect to the wall. Wakiya⁷ and Faxén^{8,9} improved the Lorentz results by incorporating the effect of the second-order reflection¹⁰. For the perpendicular direction, Brenner¹¹ derived the exact solution to the creeping equations for a spherical particle moving near a rigid wall, unrestricted by the ratio a/z . While Brenner's solution is expressed as an infinite series, approximations have been obtained through regression methods^{12,13}. For the parallel case, an exact solution valid for the entire range of z does not exist. Goldman¹⁴ and O'Neill¹⁵ derived asymptotic solutions in the limit as $z \rightarrow 0$. Perkins¹⁶ matched the series solutions to the asymptotic results ($z \rightarrow 0$) to find the friction coefficient for the entire range of z . Both Perkins' and Brenner's solutions were found to agree remarkably with experimental data¹⁷.

However, in many contexts, especially in biology, interfaces are far more complex, being neither hard, flat, nor static. Lipid membranes, which serve as critical molecular barriers between cells, represent a canonical example of complex in-

terfaces due to their intrinsic softness, lipid fluidity, and thermal fluctuations^{18–20}. Nevertheless, our understanding of how particle motion is influenced by proximity to such soft, thermally fluctuating interfaces is still in its infancy. In particular, a clear unknown is the shape of the diffusion coefficient $D_{\perp/\parallel}(z)$ as a function of the distance to the fluctuating interface z .

Recent investigations have revealed novel transport mechanisms for particles significantly larger than the molecular scales at which thermal fluctuations occur. In confined systems such as pores, theoretical and experimental studies have demonstrated that diffusion is strongly influenced by the characteristics of the fluctuating interface, leading to enhanced diffusion relative to bulk conditions, particularly for rapid or large-wavelength fluctuations of the pore walls^{21–25}. This enhanced diffusion arises from longitudinally fluctuating fluid flows, driven by the fluctuating channel walls²¹, a phenomenon reminiscent of Taylor-Aris dispersion^{23,26,27}. Yet when a particle is close to only one fluctuating interface, diffusion can be slowed down and the particle’s motion can become subdiffusive over timescales smaller than the interface relaxation timescale²⁸. Those observations suggest particle size plays a critical role in confined fluctuating systems. In addition, to fully understand the transport of smaller species, such as ions, molecules, or nanoparticles—particularly relevant in biomedical contexts—it is crucial to examine how molecular-scale transport is affected.

At molecular scales, since thermal fluctuations become significant, it is natural to expect stronger and qualitatively different transport phenomena²⁹. Theories for nanoscale hydrodynamics near interfaces are generally complex and require significant number of closures³⁰, so molecular transport processes have mostly been studied numerically. Early molecular dynamics simulations revealed that gas diffusion in microporous materials is markedly enhanced when thermal vibrations of the solid matrix are taken into account^{31,32}; the resulting increase can span several orders of magnitude, far exceeding the perturbative effects observed at larger scales^{24,33}. Similar enhancements in solvent diffusion within solid-state pores have been attributed to phonon-fluid couplings^{34–37} or extreme geometrical confinement³⁸. Conversely, hydrophilic interactions between water molecules and lipid interfaces can create local traps that suppress lateral transport^{39,40}. These studies rely on molecular dynamics simulations that explicitly incorporate the detailed molecular interactions specific to each system. This raises a broader question: what are the general principles governing molecular transport near unconfined, soft, fluctuating membranes? How do these mechanisms connect to the well-established lubrication phenomena observed at larger scales, as *e.g.* described by Eq. (1)?

In this work, we investigate the dynamics of solvent molecules near a model lipid bilayer membrane that exhibits long-range thermal fluctuations. To uncover general transport behavior, we employ mesoscale simulations based on dissipative particle dynamics (DPD), which is rooted in atomistic dynamics and can be derived directly from molecular dynamics using rigorous Mori-Zwanzig projection⁴¹. This approach enables

us to simultaneously resolve molecular motion and capture long-wavelength membrane deformations⁴². In our simulations, the space above the interface is divided into discrete layers, and statistical analyses are performed separately for particles based on the layer in which they were initially located. This allows us to measure transport properties as a function of the distance from the membrane. We mainly observe an enhancement of local diffusion in both directions near the fluctuating membrane, compared to a flat rigid wall or a wavy rigid membrane interface. Long time molecular diffusion parallel to the fluctuating membrane is also enhanced. We show that this fluidification effect is mostly due to the dynamic “wiggling” of the fluctuating membrane, by investigating several potential mechanisms. Remarkably, dynamic fluctuations transfer enough momentum to the solvent to facilitate mixing and overcome the geometrical “trapping” effect induced by the presence of wells in the membrane. Although such dynamic wiggling was shown to enhance long time, global diffusion properties only theoretically²¹, here we demonstrate this effect on *local* diffusion and show that it is significantly larger at the molecular scale than predicted by theory.

II. MODELS AND SYSTEM SETUP

A. A fluctuating membrane model

Our model membrane consists of a lipid bilayer assembly, freely fluctuating in a solvent representing water. We use a model for phosphatidylethanolamine lipids, that are frequently found in biological membranes. This phospholipid has one hydrophilic head (red dots in Fig. 1) and two hydrophobic tails (blue dots). This particular choice is not expected to affect the generality of our results. Indeed, Kranenburg et al.⁴³ found that a bilayer can always be obtained for various DPD parameters as long as the phospholipid has well-defined hydrophilic and hydrophobic parts. Further details are given in Appendix A.

The fluctuating hydrodynamics simulations are based on the DPD method^{44,45}, a particle-based Lagrangian method in which each particle represents a coarse-grained cluster of fluid molecules. Each DPD particle indexed by i is characterized by its position \mathbf{r}_i and momentum $m\mathbf{v}_i$, and its time evolution is governed by Newton’s second law of motion. Forces on particles are determined through pairwise interactions with all other particles within a cutoff distance ℓ_0 . These forces include conservative forces, in particular bond interactions to link the particles in the lipid chain. Dissipative and random forces jointly act as a thermostat, satisfying the fluctuation-dissipation theory. Repulsive force parameters are set to match the compressibility of the solvent to that of liquid water⁴⁴. For particles of different types, force parameters are determined to reproduce the mutual solubility of different species by matching the Flory–Huggins parameters⁴⁴. More details are given in Appendix B.

As system parameters, we define ℓ_0 the unit length, $k_B T$ the unit of energy and $\tau_0 = \ell_0 \sqrt{m/k_B T}$ the unit time, where m

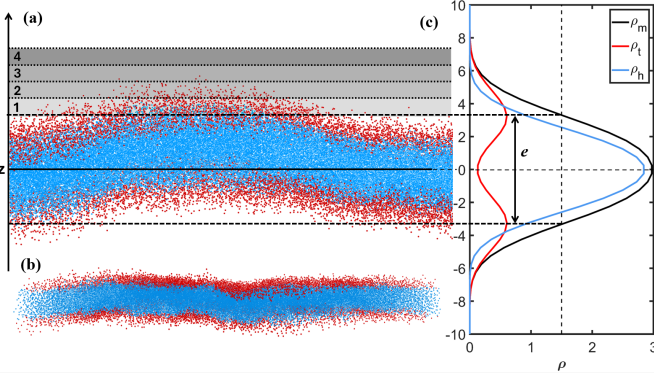


FIG. 1. (a) 2D zoomed-in cross-sectional snapshot of the fluctuating membrane, including the slabs where statistics have been performed. Points represent DPD beads, with hydrophilic heads and hydrophobic tails in red and blue, respectively. (b) Zoomed-out configuration. (c) Time-averaged density profiles with height z ($\times \ell_0$) corresponding to the membrane (black), heads (red), and tails (blue). Dashed lines (extended from (a) to (c)) show the average thickness of the membrane e , *i.e.* points where the membrane density is equal to $1.5 \ell_0^{-3}$. All spatial dimensions are in ℓ_0 unit and ρ is given in ℓ_0^{-3} .

is the mass of a bead (all the beads having the same mass). For our model system of a lipid bilayer immersed in water, $\ell_0 = 0.64 \text{ nm}$ and $\tau_0 = 3 \text{ ps}$. Every DPD bead roughly occupies the same volume as three water molecules. While there is no inherent radius a for a bead, we define twice the molecule radius $2a$ as the average distance between beads, obtained from the maximum of the solvent radial distribution function, giving $a = 0.41\ell_0$. The simulation box size is $(L_x \times L_y \times L_z) = (90.7 \times 90.7 \times 46)\ell_0^3$. With a number density $\rho = 3 \ell_0^{-3}$, the total number of DPD beads in this system is approximately 1,135,000, with approximately 10% of membrane beads. The coordinate perpendicular to the membrane is z (or \perp), whereas x and y (or \parallel) indicate interchangeably the directions parallel to the membrane. The membrane size is set to match the simulation box size, to keep the time-averaged surface tension sufficiently low. All numerical parameters are recapitulated in Appendix C.

We perform simulations using the open-source code LAMMPS⁴⁶. A modified velocity-Verlet algorithm⁴⁴ is used to integrate the DPD governing equations with time step $\Delta t = 0.01 \tau_0$. Simulations including a membrane are carried out using a pre-assembled bilayer, after an initial thermal relaxation of the membrane for 10^5 time steps. Because the coarse-grained DPD simulation still preserves the molecular structure of the fluid, from then on we refer to solvent beads as solvent molecules.

B. Structural membrane properties

Fig. 1 shows a 2D cross-sectional snapshot of the membrane and its time-averaged density profile. The thickness e of the membrane is determined by locating the z -coordinates for which the time-averaged number density is half the maximum value; here, $e = 6.70\ell_0$. At each point in time, we

project lipid tail beads on a 32×32 2D grid parallel to the membrane, and calculate their average instantaneous height $h(\mathbf{x}, t)$ per grid square, relative to the membrane midplane. The root-mean-square height fluctuations of the membrane are $\delta h = \sqrt{\langle (h(\mathbf{x}, t) - \langle h(\mathbf{x}, t) \rangle)^2 \rangle} \approx 1.3\ell_0$, where the brackets $\langle \cdot \rangle$ indicate an average over time and grid squares. Fig. 2 provides a snapshot of membrane height fluctuations at equilibrium.

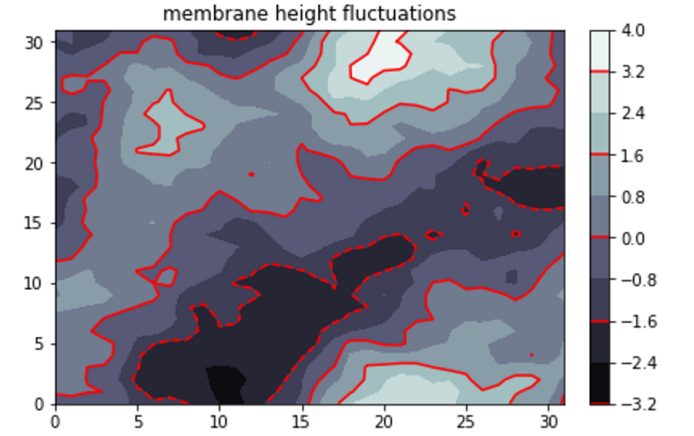


FIG. 2. Snapshot showing membrane height fluctuations, projected on a lateral (32×32) grid at time $t = 1000 \tau_0$. The color bar indicates the local height with respect to the membrane midplane in ℓ_0 unit.

To characterize the membrane "static" properties, we followed a method described in our previous work²⁸, using simulations carried out for $10^4 \tau_0$. Investigating the static structure factor of the height fluctuations, we measured a surface tension $\sigma = 0.006 k_B T / \ell_0^2$ and a bending rigidity $\kappa \approx 10 k_B T$. We also measured a stretching modulus $K_A \approx 9 k_B T / \ell_0^2$ based on the linear increase of the membrane surface tension with the area per lipid. Here, κ and K_A are smaller than in our previous work²⁸ because the solubility mismatch between solvent and hydrophobic beads is smaller here ($\Delta a_{ij} = 26$ compared to $\Delta a_{ij} = 55$).

C. Statistical analysis per slab

In this work, we focus on solvent dynamics as a function of the distance to the interface. One common challenge for such data analysis is that the solvent residence time at a certain distance from the membrane is short, reducing statistical accuracy. To circumvent this it is common to perform statistics on particle trajectories that start in a given layer (conditional probability)⁴⁷. We thus divide the simulation domain into slabs parallel to the interface, as sketched in Fig. 1. The slab thickness is equal to ℓ_0 , which we recall corresponds to the cut-off distance for the DPD forces. A slab's thickness is thus close to the intermolecular distance $2a \simeq 0.82\ell_0$. Thus, a solvent molecule meets several neighbors during its stay in a slab. The bottom edge of the first slab corresponds to the coordinate z where the number density of the solvent is equal to half that in the

bulk, $1.5\ell_0^{-3}$ (dashed lines in Fig. 1c). In each simulation, the statistical quantities computed in a given slab are performed on the molecules that were located in that slab at start of the simulation – but after the thermalization process.

D. Comparison with other interfaces

To disentangle the effects of membrane shape and dynamics, we conducted simulations of solvent dynamics near three interfaces with identical simulation domains: (a) the fluctuating membrane, (b) a rigid undulated membrane, and (c) a flat rigid wall. To prepare (b), the fluctuating membrane beads are frozen after an initial relaxation (10^5 time steps) by excluding them from time integration and setting their velocity to zero. The flat rigid wall in case (c) was generated by randomly placing wall beads with a similar number density of $\rho = 3 \ell_0^{-3}$ within a “wall” volume spanning the simulation domain horizontally and with a thickness $e = 6.7\ell_0$ similar to the thickness of the fluctuating membrane. After a relaxation process of 5000 time steps, the wall beads were excluded from time integration, and their velocities were set to zero. The interaction parameters between the solvent molecules and the flat wall beads were set equal to that between the solvent molecules and the hydrophilic lipid beads. As a consequence, the solvent slightly penetrates the flat wall after the thermalization process, akin to the penetration that occurs on the surface of the membrane.

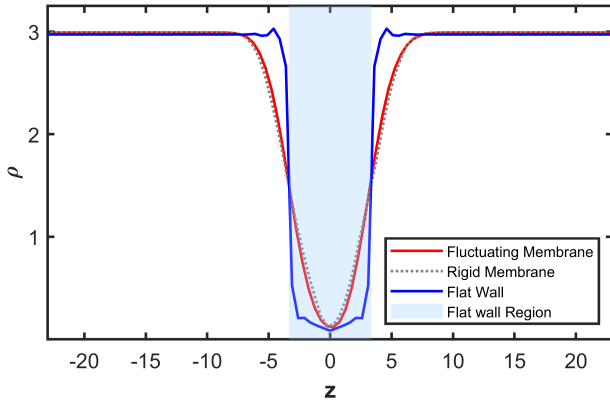


FIG. 3. Time-averaged density profile of solvent molecules in the presence of a fluctuating membrane (solid red), flat rigid wall (dashed blue) or a rigid membrane (dotted gray). The coordinate z is indicated in ℓ_0 unit. Gray and red lines have significant overlap. The shaded region indicates the thickness of the flat wall and the average position of the membrane surfaces, where the density of solvent molecules is half that in the bulk.

Fig. 3 shows the solvent density profiles, averaged along the parallel directions and over time, for the 3 different cases. Profile points are obtained along z within slabs of thickness $0.5 \ell_0$. The solvent density profile varies sharply near the flat interface, indicating a clear separation between the solid and fluid phases. In comparison, the solvent density profiles vary smoothly near the membrane surfaces since the solvent can occupy open volume regions within wells of the membrane,

while it is evacuated from the bumpy regions. The profiles are almost identical for the fluctuating (in red) and rigid (in dashed gray) membranes, which indicates that dynamic events associated with the membrane fluctuations do not impact the solvent density on average.

We now turn to examine the dynamics of solvent molecules.

III. BROWNIAN MOTION OF THE SOLVENT MOLECULES IS ENHANCED NEAR A FLUCTUATING MEMBRANE.

A. Mean-squared displacement of solvent molecules: from ballistic to diffusive

To characterize Brownian motion of the solvent molecules near the different interfaces, we first consider their mean-square displacement (MSD) in each direction as

$$\text{MSD}_{\perp,\parallel}(t) = \langle |\mathbf{r}_{\perp,\parallel}(t) - \mathbf{r}_{\perp,\parallel}(0)|^2 \rangle, \quad (2)$$

where $\langle \cdot \rangle$ denotes an average on molecules and on moving time windows. Fig. 4 displays the MSD of the molecules in the perpendicular and parallel directions near the fluctuating membranes. The different shades of red correspond to the different slabs, so to molecules which started their motion at different distances from the fluctuating membrane. Similar profiles are obtained near the flat and rigid membranes (not shown here). As reference we also show the MSD for a bulk simulation in black.

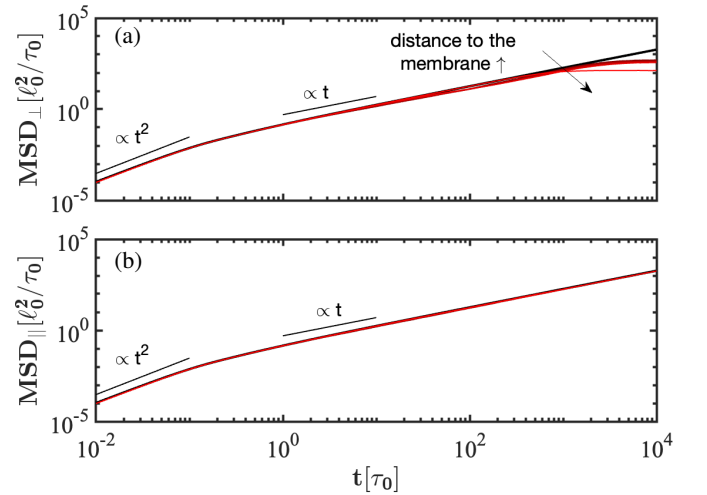


FIG. 4. Mean square displacement (MSD) of solvent molecules near the membrane in the perpendicular (a) and parallel (b) directions. Red lines (almost superimposed), from darkest to lightest, represent slabs at distances of 0.5, 1.5, 2.5, 3.5, 4.5 and $19.5 \ell_0$ from the fluctuating membrane surface. Black lines indicate the bulk case.

Fig. 4 shows that the MSDs follow 2 different power-laws in time, which are apparent for all slabs and for the bulk case, in both direction. Motion is ballistic and then around $t \simeq \tau_{\text{diff}} \simeq 1 \tau_0$, transitions to a diffusive regime. At long

times, $\text{MSD}_\perp(t)$ tends to a plateau, a signature of confinement between the interface and its periodic image. From the time scale $\tau_{\text{conf}} \simeq 10^3 - 10^4 \tau_0$ at which the plateau emerges, we conclude that the investigation of the diffusive dynamics in the perpendicular direction is appropriate for $t < \tau_{\text{conf}}$. At long times, we can quantify the self-diffusion coefficient of the solvent in the parallel direction, as

$$D_\parallel^\infty = \lim_{t \rightarrow \infty} \frac{\text{MSD}_\parallel(t)}{2t}. \quad (3)$$

For the bulk case, motion is isotropic and we find $D_b \equiv D_\parallel^\infty = 0.092 \ell_0^2/\tau_0$. The time to diffuse the characteristic distance $2a$ between two molecules is $(2a)^2/D_b \simeq 7 \tau_0$, which is comparable to the time required to transition to the diffusive regime τ_{diff} . The time to diffuse the vertical distance between periodic membranes is $(L_z - e)^2/D_b \simeq 10^4 \tau_0$ which is indeed comparable to τ_{conf} .

Already at this level of description, the molecular nature of the investigation is apparent. The Stokes-Einstein relation in the bulk estimates a diffusion coefficient $k_B T / 6\pi\eta a \simeq 0.046 \ell_0^2/\tau_0$, where the dynamic viscosity $\eta = m\rho v$ and $v = 0.94 \ell_0^2/\tau_0$ was measured from non equilibrium simulations under an applied shear stress (see Appendix D). This estimate is 2 times smaller than the measured D_b , a result which was also obtained in DPD simulations by Pan et al.⁴⁸ or in MD simulations⁴⁹. This discrepancy may not be explained by inertial effects since the Schmidt number $\text{Sc} = v/D_b = 10.18$ is sufficiently high that momentum in the fluid diffuses much faster than the fluid molecules themselves⁵⁰. Rather, the discrepancy is attributable to molecular effects, since the Stokes-Einstein relation is only valid in the continuum limit. Modifications of the relation to account for the molecular fluid nature, for instance attributed to wave-number dependencies of the viscosity coefficient or effective slip at the particle's surface could yield a modified Stokes-Einstein estimate closer to the measured value^{49,51-53}.

| | $D_\parallel^\infty [\ell_0^2/\tau_0]$ | D_\parallel^∞ / D_b |
|----------------------|--|----------------------------|
| fluctuating membrane | 0.0897 | 0.975 |
| flat wall | 0.0875 | 0.951 |
| rigid membrane | 0.0859 | 0.934 |

TABLE I. Diffusion coefficient of the solvent molecules D_\parallel^∞ , in the presence of an interface.

Table I summarizes the value of D_\parallel^∞ near different interfaces, averaged over the six closest slabs to the interface. Note that at long times, the molecules would have explored the space between the interface and its periodic image. Overall, confined molecules are less mobile than in the bulk – the interface contributes to an increased friction which reduces the diffusion coefficient. This reduction (the plateau value) depends on the system considered: the diffusion is less reduced in the fluctuating membrane case than by the rigid membrane. The fluctuating membrane thus appears to “fluidify” motion near its interface.

We now turn to a more detailed time analysis.

B. Time-dependent diffusive properties as molecules navigate close to the interface

To explore the mobility of the molecules near the interface, while excluding the average drift away from the interface (discussed in Sec. IV A), we calculate their local, time-dependent, diffusion, through the expression

$$D_{\perp,\parallel}(t) = \frac{1}{2} \frac{\sigma_{\perp,\parallel}^2(t)}{t} \quad (4)$$

where $\sigma_{\perp,\parallel}^2(t)$ is the standard deviation (STD) of the molecules' displacements in each slab, *i.e.* where any short time drift contribution is removed.

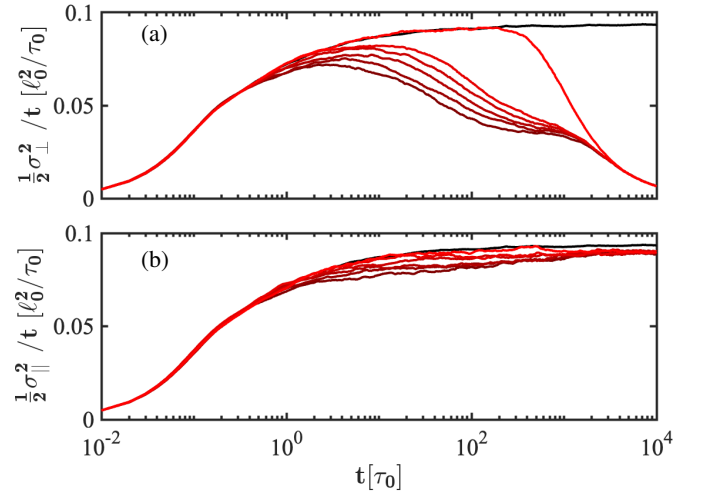


FIG. 5. Time evolution of $\frac{1}{2} \frac{\sigma_{\perp,\parallel}^2(t)}{t}$ in the (a) perpendicular and (b) parallel directions. Red lines, from darkest to lightest, represent slabs at distances of 0.5, 1.5, 2.5, 3.5, 4.5 and 19.5 ℓ_0 from the fluctuating membrane surface. Black lines indicate the bulk case.

Fig. 5 displays $D_{\perp,\parallel}(t)$ for different slabs near the fluctuating membrane. At this level, the features of $D_{\perp,\parallel}(t)$ are similar for the rigid and flat cases (see Appendix E) and so we focus on the fluctuating membrane. In the perpendicular direction, diffusive motion exhibits several stages. The diffusion coefficient D_\perp first increases before reaching a quasi plateau around $t \simeq 1 - 10 \tau_0$, corresponding to the onset of the diffusive regime. This time increases slightly with increasing distance from the interface. A molecule starting closer to the interface is more likely to reach a stationary regime sooner as it will more quickly probe the domains closer to the interface. Diffusive motion is then quickly hindered around $t \simeq 10 - 100 \tau_0$, at a timescale again increasing with increasing distance from the interface. Perpendicular mobility is reduced because perpendicular motion is bounded by the interface, which is again, reached sooner for molecules starting closer to the interface. The characteristic time scale to diffuse vertically across a slab is $\tau_{\text{slab}} = \ell_0^2/D_b^\infty \simeq 10 \tau_0$, and indeed,

for the first slab (darkest color), molecular mobility decays around τ_{slab} . Eventually perpendicular mobility decays to zero at very long times $t \simeq 10^4 \tau_0 \simeq \tau_{\text{conf}}$, due to effective confinement as all molecules sense the interface's periodic image.

In the parallel direction, D_{\parallel} , much like D_{\perp} , experiences a quasi-plateau around $t \simeq 1 - 10 \tau_0$; this quasi-plateau is more or less clear depending on the distance from the interface. Eventually at long times, as molecules sense the entire vertical domain, D_{\parallel} reaches another plateau which corresponds to D_{\parallel}^{∞} .

C. Spatially-dependent diffusive properties

To compare the dynamics in different systems, we characterize Brownian motion by a single diffusion coefficient in each slab. Specifically, we choose to focus on $D_{\perp/\parallel}(t_d)$, taking $\tau_{\text{diff}} < t_d < \tau_{\text{slab}}$ after the onset of the diffusive regime but before significant diffusion in between slabs. For parallel diffusion we set $t_d = 10 \tau_0$, and for orthogonal diffusion, t_d corresponds to the maximum of $D_{\perp}(t)$ in each slab, which is $\approx 10 \tau_0$. For simplicity, we write $D_{\perp/\parallel} = D_{\perp/\parallel}(t_d)$. To increase statistical accuracy, the results for $D_{\perp/\parallel}$ are averaged over 10 independent simulations.

The diffusion coefficients $D_{\perp/\parallel}$ in each slab at height z above the interface are displayed in Fig. 6. Close to the interface, both diffusion coefficients are reduced in all systems explored. Far from the interface, values approach the bulk diffusion coefficient D_b , without being strictly equal to D_b due to the small but finite confinement of the solvent in the z direction.

A few striking differences should be noted between the different systems. The reduction of D_{\perp} near a flat rigid wall is steep, with a sharp decrease between the 1st and 2nd slabs, and where significant mobility reduction is observed until $\mathcal{L}_{\text{HI}} = 4 - 5 \ell_0$. In contrast, the mobility reduction near a rigid or fluctuating membrane is smoother, continuously decreasing over 4-5 slabs, with the same slope including in the 1st and 2nd slabs. D_{\perp} is smallest in the rigid membrane case for nearly the entire range, except in the 1st slab. The mobility in the fluctuating membrane case is always larger than the rigid membrane case, and even larger than near the flat wall on the 1st and 2nd slabs. This is consistent again with a fluidification effect of the fluctuating membrane. Similar conclusions can be made in the parallel direction, with however an overall smaller reduction of the diffusion coefficient in that case.

To gain phenomenological insights, the mobility reduction near the flat wall can be compared with familiar, continuum lubrication theories. Fig. 6 displays the diffusion coefficient calculated from Brenner's theory near a hard wall (cyan lines), whose simplified expression reduces to Eq. (1) to first order in a/z , where a is the molecule's radius. The applicability of Brenner's theory to molecular motion is limited since equations are derived in the continuum limit. Nonetheless, we choose $a = 0.41 \ell_0$ as an order of magnitude and compare qualitatively the results. Strikingly, the shape of the prediction,

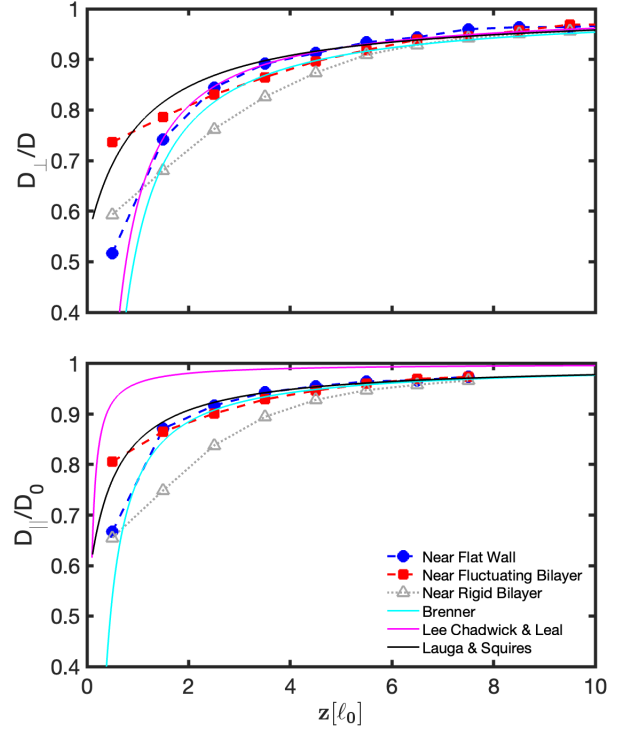


FIG. 6. Profiles of the diffusion coefficients D_{\perp} and D_{\parallel} as a function of the distance to the interface. Symbols are from the present simulations. Solid cyan (resp. magenta) lines are obtained from Brenner, Eq. (1) (resp. Ref. [54]) who considered the motion of a solid particle moving near a flat wall (resp. a flat liquid interface). The black lines are obtained from Eq. (5) with $\ell_s = \ell_0$.

with a sharp decrease near the interface (cyan), is in excellent agreement with both diffusion coefficients $D_{\perp}(z)$ and $D_{\parallel}(z)$ for the flat wall (blue circles). This suggests that qualitative insights on diffusive motion near a flat wall can be transferred from finite size solid particles translating in a viscous fluid to small molecules with no specific physico-chemical interactions.

The fluidification effect near the fluctuating membrane has similar effects as an apparent slip at the interface. Inspired by the work of Olsen et al.⁵⁵ who studied the diffusive motion of lipid nanoparticles near a lipid membrane, we can write the diffusion coefficient in the form of Brenner's law, accounting for an apparent slip length ℓ_s at the interface following a theory by Lauga and Squires⁵⁶ as:

$$\frac{D_{\perp}(z)}{D_b} = 1 - \frac{9}{8} \frac{a}{z + \ell_s} \quad \text{and} \quad \frac{D_{\parallel}(z)}{D_b} = 1 - \frac{9}{16} \frac{a}{z + \ell_s}. \quad (5)$$

The diffusion profiles associated with Eq. (5) are plotted in Fig. 6 in black, assuming $\ell_s = \ell_0$. The theoretical profiles with slip are significantly flattened near the interface, and agree with simulations of the fluctuating membrane. Molecular motion near a bilayer can thus be described with an effective finite slip. Although the slip length $\ell_s = \ell_0 = 0.64 \text{ nm}$ is small compared to measured slip lengths in experimental systems, which are more on the order of 10 nm at least^{57,58},

the slip length scale is relevant in our system as it is similar to that of the characteristic height of membrane corrugations $\delta h = 1.3 \ell_0$. Near the rigid membrane, however, such an approach fails to predict diffusive motion, for any slip length.

IV. MECHANISMS RESPONSIBLE FOR THE FLUIDIFICATION OF MOLECULAR MOTION NEAR WIGGLY INTERFACES

We seek to understand the mechanisms underlying our observations in Sec. III. Overall, the fluidification of motion near the fluctuating membrane could be due to several effects: (A) geometry: the membranes display wells and humps that could locally modify motion; (B) wiggleness: as the membrane moves, it could push groups of solvent molecules, inducing flows that could help mixing^{21,22}; (C) liquid aspect of the membrane: lipids can diffuse freely in the fluctuating case, lowering the stresses at the interface; (D) elasticity of the membrane could induce memory effects and modify friction in various ways^{33,59}. Our goal is now to test these different mechanisms.

A. Membrane wells act as traps; the wavy geometry creates an effectively “smoother interface”.

The density profiles in Figs. 1 and 3 show that molecules near membranes can reside in deeper positions compared to the flat wall. These correspond to membrane wells, located in regions of negative height fluctuation (see Fig. 2). Several of our observations suggest geometry, *i.e.* the presence of wells and bumps in a membrane, hinders motion: indeed, in the rigid membrane case, both D_{\parallel}^{∞} and the local mobility $D_{\parallel,\perp}(z)$ are reduced compared to the flat and fluctuating cases. We hypothesize that this is due to a “trapping effect”. Many theories demonstrated that the long-time diffusion coefficient of particles should be decreased by the constrictions which form effective “entropic” barriers, where a particle spends a long time exploring wells before it can escape that well^{60–64}. This effect has only been proven to act on D_{\parallel}^{∞} but here we find it, naturally, also has an effect on local mobility $D_{\perp,\parallel}(z)$.

To add further proof to this trapping hypothesis, we analyze orthogonal displacements relative to the membrane, $\langle \delta z(t) \rangle = \langle z(t) - z(0) \rangle$, for each slab, see Fig. 7. The mean displacement remains positive in time, indicating a clear repulsion of molecules away from the interface. The closer the solvent molecules to the interface, the earlier and the stronger the repulsion. Near the flat wall (blue), the mean displacement is larger in the first two layers than near the membranes (gray/red). Similar conclusions may be drawn from the probability distribution functions of vertical displacements (see Appendix F). The displacement being comparable near both membranes is consistent with the presence of wells close to the interface where molecules stay for long times and are not repelled as efficiently far from the interface. This increases local friction, and explains the discrepancies in the mobility

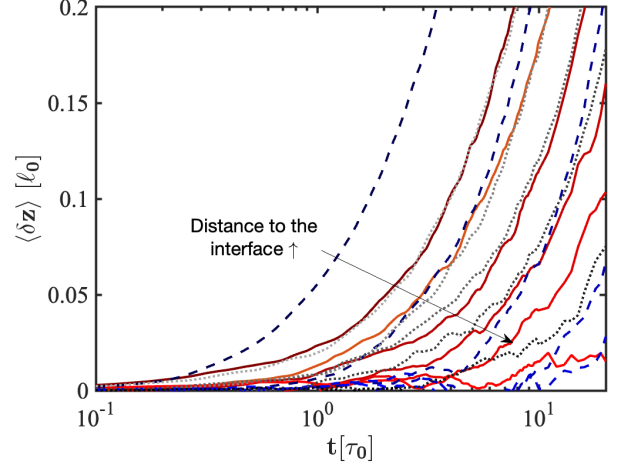


FIG. 7. Mean perpendicular displacement of solvent molecules with time. Same color code as Fig. 5.

measurements between the rigid membrane and the flat wall cases. It also illustrates that measurements of dynamic properties near a membrane are averaged over the lateral direction, and so averaged over wells and bumps, creating an effectively “smoother” landscape vertically.

Geometry thus has 2 effects: (i) membrane wells act as traps – molecular drift away from the interface is slowed down compared to near a flat surface – increasing local and global friction and (ii) the wavy geometry creates an effectively “smoother interface”.

B. Dynamical fluctuations kick solvent molecules

Although solvent molecules near the fluctuating membrane should experience increased friction due to membrane geometry, like near the rigid membrane, motion is clearly facilitated in this fluctuating case. Compared to other cases, the fluctuating membrane continuously experiences fluctuations of thermal origin that emerge and relax. This is consistent with a transfer of momentum hypothesis, where the motion of the membrane itself agitates molecules and facilitates mixing.

To test this hypothesis, we first characterize the relaxation dynamics of the fluctuating membrane and then see how they relate to molecular diffusion. For each fluctuating mode q in Fourier space, we calculate the height autocorrelation function $F(q, t) = \langle \tilde{h}(q, t) \tilde{h}^*(q, 0) \rangle$ where $\tilde{h}(q, t)$ is the Fourier transform of $h(x, t)$ (see Appendix G). The decay of $F(q, t)$ for different modes q shown in Fig. 8a is not purely exponential. This trend has been observed in previous lipid bilayer studies, and described via stretched exponential⁶⁵ or double exponential^{66,67} models. To simplify, we characterize $F(q, t)$ by a “global” relaxation time scale⁶⁵, as

$$\tau_r(q) = 2 \int_0^\infty \frac{F(q, t)^2}{F(q, 0)^2} dt. \quad (6)$$

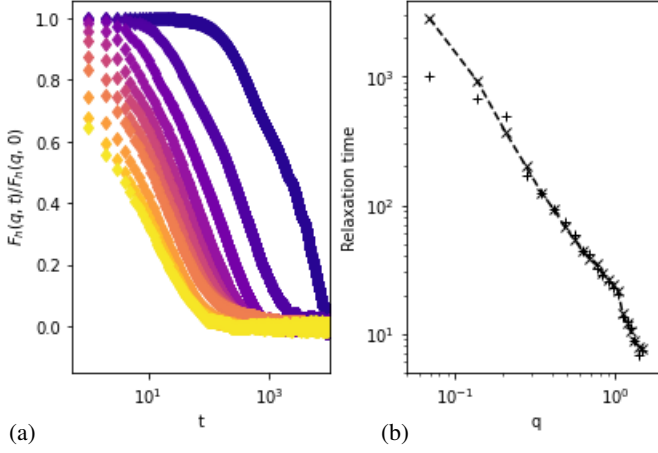


FIG. 8. a) Time decay of the autocorrelation function $F(q, t)$, for modes with wavenumber $q = n_q q_1$ where $q_1 = 0.069 \ell_0^{-1}$ is the smallest wavenumber and n_q denotes odd numbers between 1 and 21 (from purple to yellow). b) Relaxation time $\tau_r(q)$ of the membrane fluctuations, calculated from Eq. (6). + and \times symbols correspond to simulations lasting for $10^4 \tau_0$ and $15 \times 10^4 \tau_0$, respectively, demonstrating the profile is converged. Times are given in τ_0 units and q as $1/\ell_0$.

The relaxation time $\tau_r(q)$ decays with increasing wavenumber q , see Fig. 8b, reaching values between $10 - 10^3 \tau_0$.

How does this relaxation time relate compare with other relevant timescales? As the membrane fluctuations occur over multiple length scales, inspired by Marbach et al.²¹, we build a dimensionless Péclet number as the ratio of a characteristic diffusive time scale $\tau_{\text{diff}}(q) = 1/D_b q^2$ across a characteristic length scale $1/q$ compared with the relaxation time at that scale

$$\text{Pe} = \frac{\tau_{\text{diff}}(q)}{\tau_r(q)} = \frac{1}{D_b q^2 \tau_r(q)}.$$

We use $D_b \simeq 0.1 \ell_0^2/\tau_0$ as an order of magnitude, and reading off Fig. 8b, we find membrane fluctuations typically exhibit $\text{Pe} \simeq 1$, independently of the fluctuation length scale. Dynamic membrane fluctuations thus act on similar time and length scales as purely diffusive motion and thus can potentially affect overall mobility.

Convective mixing induced by dynamic fluctuations has been shown theoretically²¹ to modify long time parallel diffusion in confined media D_{\parallel}^{∞} . When the Péclet number $\text{Pe} \gtrsim 1$ (respectively $\text{Pe} \lesssim 1$), D_{\parallel}^{∞} is enhanced (respectively decreased) compared to a flat wall case. For $\text{Pe} \simeq 1$, the outcome is not obvious, and thus it is remarkable that fluctuations here are sufficient to enhance D_{\parallel}^{∞} compared to the flat wall case. The rigid membrane case corresponds to infinite relaxation times $\tau(q) = \infty$, thus to $\text{Pe} \rightarrow 0$, and reduced diffusion, which is consistent with our study, and with the “trapping effect” of geometry. In this theory, the factor $2\delta h^2/H^2$ quantifies the change in diffusion coefficient where δh is the amplitude of the interface corrugations and H the distance between the confining interfaces. Here $\delta h = 1.3 \ell_0$ and $H = 46 \ell_0$ giving

a relative change of 0.04%, which is much smaller than the observed differences of about 2% in Table I. The discrepancies between the theory and our observations are likely due to molecular effects, since Ref. [21] is only valid for much larger particles than the solvent. Yet, qualitatively the effects are similar: purely spatial corrugations of the confining domain reduce motion by trapping them, while local membrane motion kicks molecules and facilitates their motion.

The theory in Ref. [21] does not provide insights on local diffusion, so as to explain the trends in Fig. 6. Nonetheless, we can still expect similar effects are at play and well described by the Péclet number. For large wavenumbers, $\tau_r(q \simeq 1 \ell_0^{-1}) \simeq 10 \tau_0$, which is of the order of the diffusion time scale of the solvent molecules over a slab τ_{slab} . Thus, a molecule diffusing near the membrane, experiences several local wiggly movements of the membrane before moving away. This coupling between the molecular motion and the quick membrane fluctuations likely explains the fluidification effect of diffusive motion at small z near the fluctuating interface.

C. Membrane fluidity itself is likely not at play

Another major difference between the rigid and fluctuating membrane is that lipids are free to diffuse in the fluctuating case. This could possibly facilitate lateral motion by reducing local stress. The lipid molecules are much larger than the solvent molecules, and the ratio of the lipid lateral diffusion coefficient within the membrane (D_l) and the solvent diffusion coefficient (D_b) is quite small, $D_l/D_b \simeq 0.01$, in agreement with previous findings⁶⁸. This suggests that lipid fluidity operates on timescales that are much larger than that of local diffusion, and hence are likely playing a minor role.

To push this reasoning slightly further, we present in Fig. 6 a theory (in magenta) corresponding to the motion of a sphere near a non-deformable liquid-liquid interface, from Lee et al.⁵⁴, where

$$\frac{D_{\perp}(z)}{D_b} \simeq 1 - \frac{15}{16} \frac{a}{z} \quad \text{and} \quad \frac{D_{\parallel}(z)}{D_b} \simeq 1 - \frac{3}{32} \frac{a}{z}. \quad (7)$$

The predictions using Eq. (7) yield similar profiles for $D_{\perp}(z)$ versus Brenner’s with the same radius, but quite different for $D_{\parallel}(z)$, demonstrating lateral fluidity should primarily facilitate only lateral motion. In contrast, the behavior for all simulated cases are quite similar in the tangential and perpendicular directions. The fluidification effects we observe in the fluctuating case are thus different from stress reduction mechanisms near a fluid interface.

D. Lack of elastic effects in the diffusive regime

Finally, we investigate whether the molecules near the membrane experience elastic forces originating from the deformability of the fluctuating membrane. Inspired by Ref. [33], we assume that at distance z from the interface, the mean forces

on a molecule can be decomposed into a thermal force associated with the equilibrium density distribution $F_{\text{eq}}(z)$ – reflecting intermolecular interactions –, a drag force resisting molecule drift away from the interface $F_{\text{drag}}(z)$, spurious drift arising from the coupling between random motion and the dependence of molecule mobility on the distance to the interface $F_{\text{mn}}(z)$, and finally a non-conservative interaction force $F_{\text{int}}(z)$ with the interface. The different contributions originate from an overdamped Langevin equation for particle motion. Our simulations allow us to measure all *conservative* forces, *i.e.* all forces but $F_{\text{int}}(z)$. With these measurements we demonstrate $F_{\text{eq}}(z) + F_{\text{drag}}(z) + F_{\text{mn}}(z) = 0$ (see Fig. 17 and details in Appendix H) and so the absence of non-conservative forces in our case.

Soft non-conservative forces have been observed experimentally for a colloidal drop near a wall³³ and theoretically for a particle near an elastic membrane⁵⁹. However, we do not observe them here. This apparent paradox relates to the size of the diffusing object and the time scale of observation. Indeed, such soft forces are only present at “short” timescales. In Ref. [33] the non conservative forces appeared at a time scale of the order of 0.01 – 1 s for a micron-sized particle. The diffusion coefficient near the interface is $D_{\parallel} \simeq 0.1 \mu\text{m}^2/\text{s}$ which amounts to a diffusion timescale across the particle size of about 3 s. Therefore, in the case of molecular diffusion near the fluctuating membrane, if present, the non-conservative forces are expected to occur at timescales shorter than the time to diffuse across a molecule’s diameter, and so in the ballistic regime. They thus have no effect in the diffusive regime.

V. DISCUSSION AND CONCLUDING REMARKS

We have probed numerically the diffusive motion of solvent molecules, in the parallel and perpendicular directions near 3 different interfaces. Our observations are best recapitulated by noticing the different length scales at play, which correspond to the different mechanisms unveiled – see Fig. 9.

Near a flat wall, as reference, we found that the molecules local diffusion coefficient is reduced, and that this reduction can be described by continuum theories for the mobility reduction of a solid particle of size a near a flat solid wall. Here we estimated the characteristic radius a of a DPD molecule – typically representing 3 “real” water molecules – as half the distance at which the radial pair distribution function of the solvent peaks. The “hydrodynamic” length scale measuring the distance over which mobility reduction is observed is $\mathcal{L}_{\text{HI}} \simeq 5 \ell_0 \approx 12 a$.

In comparison, we explored molecular motion near a membrane made of lipid self-assembly. The membrane average height fluctuations with respect to the membrane midplane are $\delta h = 1.3 \ell_0$, whereas local maxima or minima of the membrane reach $h_{\text{max}} \approx 3 - 4 \ell_0$. Near the rigid, or frozen in time, membrane, we found a reduction of local solvent mobility and of long-time parallel diffusion, compared to the rigid case. We suggest that the membrane’s wavy geometry, creates wells that act as local traps for motion, significantly reducing mobil-

ity compared to a flat case. Since $h_{\text{max}} \simeq \mathcal{L}_{\text{HI}}$ we can expect that the hydrodynamic mobility reduction occurs over a similar length scale as the “trapping” effect, which was indeed measured in our case. Overall, trapping reduces the long-time parallel diffusion as well.

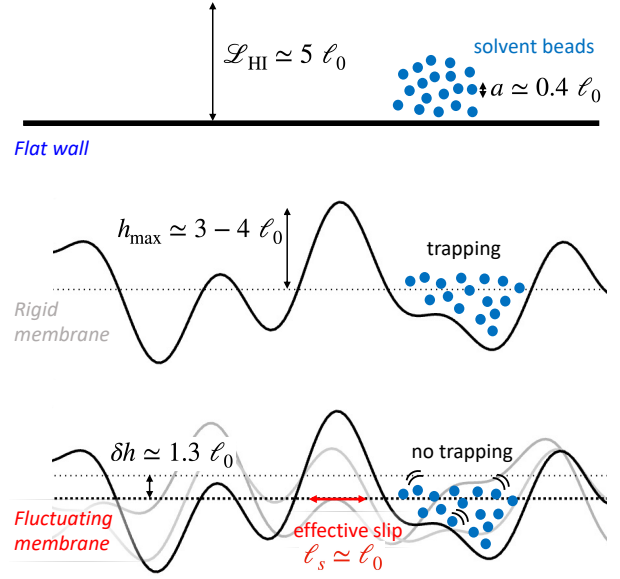


FIG. 9. Schematic summary of the mechanisms influencing molecular mobility near the different interfaces, and associated length scales. Solvent molecules are trapped in the wells of the rigid membrane, while dynamic membrane fluctuations help them explore beyond the wells. See text for details.

In the fluctuating case, when the membrane experiences spontaneous thermal motion, we found local mobility is comparable to the flat wall case, and even facilitated in the layer that is the closest to the membrane. We estimated the length scale of this fluidification effect through an effective slip length $\ell_s \approx \ell_0$, which is close to the characteristic magnitude of height fluctuations δh . Through an evaluation of the ratio between the time to diffuse across a wave, and the relaxation time of that wave, we found that dynamic kicks of the fluctuating membrane increase molecular agitation. This conclusion is conformed by the remarkable similarity between ℓ_s and δh , showing that fluidification is likely promoted over a length scale that is comparable to the mean membrane fluctuations. Several phenomena are not expected to be at play, such as lipid mobility within the membrane or elastic effects which respectively occur on timescales that are much longer or shorter than the timescales relevant for diffusive motion at this molecular level.

While we have probed individual dynamic properties, such as the self-diffusion coefficient of the molecules, it is natural to ask how other dynamic properties may be modified near soft fluctuating interfaces. For instance, a recent numerical investigation demonstrated that the flexibility of a porous matrix can allow for enhanced permeability by deforming the local structure⁶⁹. Other “fluctuating aspects” such as longitudinal vibration modes of a flat surface (phonons) have been shown theo-

retically and experimentally to modify hydrodynamic friction and electronic currents in the surface^{70,71}. Soft and/or fluctuating interfaces thus exhibit exotic consequences on varied dynamical properties.

As an illustration, we briefly investigate in our system a canonical collective dynamic quantity, the center of mass (COM) of the solvent, see Fig. 10. In the parallel direction, the COM diffuses in the domain bounded by the flat wall or the rigid membrane, whereas it is significantly slowed down in the fluctuating membrane case. This is surprising as we have found individual diffusion is mostly accelerated by the presence of fluctuations. The center of mass diffusion coefficient in a slit can be modeled⁷² as $D_{\text{com}} = k_B T H / 12 \eta L W = 1.6 \times 10^{-4} \ell_0^2 / \tau_0$ and Fig. 10 displays, in black, the theoretical position of the COM as $y = y_0 + \sqrt{2 D_{\text{com}} t}$. This prediction is in remarkable agreement with the flat and rigid membrane cases, for which we can estimate $D_{\text{com}} \simeq 10^{-4} \ell_0^2 / \tau_0$. The drastic slow down induced by fluctuations could be hypothesized to be due to the effective slip. Adding slip boundary conditions on the interface modifies the COM diffusion coefficient⁷², by a factor $(1 + 6\ell_s/H)$. This factor is small, since $\ell_s \simeq \ell_0$, and it is always greater than 1, thus contributing to enhance diffusion, opposite to the observed trend. Another phenomenon must be at play! Collective dynamic properties near fluctuating interfaces thus hold many more mysteries to be rationalized.

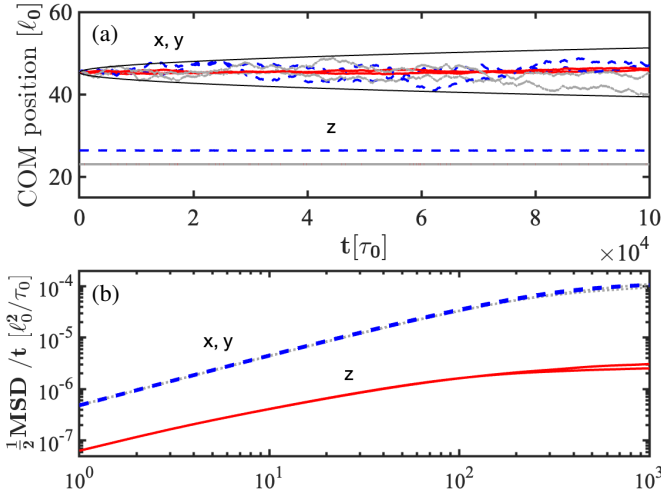


FIG. 10. Temporal evolution of a) the solvent center of mass and b) its half MSD over time, near a fluctuating membrane (solid red), a rigid membrane (dotted gray) and a flat wall (dashed blue). The direction of motion is indicated on the figure. The black lines in a) correspond to $y = y_0 + \sqrt{2 D_{\text{DB}} t}$.

This work brings some insights into apparent models of the motion of fluids confined by a soft interface, where the diffusion, and subsequently the viscosity, would depend on the distance to the interface. A still open question of interest is the impact of interface fluctuations on the friction coefficient or slip of the fluid at the interface⁷³, and how this couples with the change in diffusion.

ACKNOWLEDGMENTS

The authors acknowledge fruitful discussions with Benoit Coasne, Amael Obliger, Jean-Louis Barrat and Aleksandar Donev. This work was granted access to the HPC resources of IDRIS under the allocations 2024-[A0152A12031] made by GENCI, and to computational resources provided by the computing meso-centre CALMIP under project No. P1002. S.M. and M.A. acknowledge financial support from the CNRS through the MITI interdisciplinary program (MembranesJumelles). A.M and Z.L. acknowledge the financial support from the National Science Foundation via grants OAC-2103967 and CDS&E-2204011.

Appendix A: Lipid and water simulation model

The system we model comprises phosphatidylethanolamine (PE) and water. The structure of PE consists of two C_{15} hydrocarbon chains attached to a glycerol group. Following the approach of Groot and Rabone⁶⁸, 3 carbon atoms are grouped into one DPD bead of type **c**, while each bead of type **e** represents 1.5 glycerol-linking unit. The PE molecule and its mapping to the coarse-grained DPD model are shown in Fig. 11. The association between the numerical and physical systems is mainly done through the number density of water molecules which is given by $\rho = N_A \rho_w / M_w$, where N_A is the Avogadro constant, and ρ_w and M_w are the density and molar mass of water, respectively.

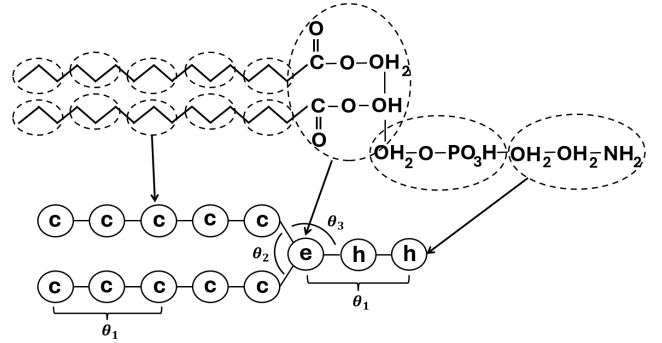


FIG. 11. Phosphatidylethanolamine (lipid) molecule and its coarse-grained representation.

Based on the partial volumes of $(CH_2)_3$ and the glycerol-linking molecule, as reported by Lu et al.⁷⁴, Groot and Rabone determined that both type **c** and type **e** DPD beads correspond to a volume of 90 \AA^3 . The volume of a water molecule is approximately 30 \AA^3 ; thus, each water DPD bead (type **w**) represents three water molecules.

With the number density of DPD beads $\rho = 3$, and the coarse-graining parameter $N_m = 3$, the reference length scale of the system $\ell_0 = \sqrt[3]{N_m \times \rho \times 30 \text{ \AA}^3} = 6.46 \text{ \AA}$. The mass of each DPD bead is given by $m = N_m \times \frac{M_w}{N_A} \approx 9 \times 10^{-26} \text{ kg}$, where $M_w = 18 \text{ g/mol}$ is the molar mass of water, and $N_A = 6.022 \times$

10^{23} mol^{-1} is Avogadro number. Given the reference temperature $T = 300 \text{ K}$, and Boltzmann constant $k_B = 1.38 \times 10^{-23} \text{ J/K}$, the reference time scale $\tau_0 = \ell_0 \sqrt{m/k_B T} = 3 \text{ ps}$.

Appendix B: Dissipative Particle Dynamics method

In Dissipative Particle Dynamics, each DPD bead i is characterized by its position and momentum, where time evolution is governed by momentum and energy conservation, as described by the following set of equations⁴⁴:

$$\begin{aligned} \frac{d\mathbf{r}_i}{dt} &= \mathbf{v}_i, \\ m_i \frac{d\mathbf{v}_i}{dt} &= \mathbf{F}_i = \sum_{j \neq i} (\mathbf{F}_{ij}^C + \mathbf{F}_{ij}^D + \mathbf{F}_{ij}^R). \end{aligned}$$

Here, m_i represents the mass of bead i , t represents time, while \mathbf{r}_i , \mathbf{v}_i , and \mathbf{F}_i denote the position, velocity, and force vectors of bead i , respectively. The summation is performed on all other beads within a cutoff radius $r_c \equiv \ell_0$. The three pairwise components of \mathbf{F}_i , the conservative force \mathbf{F}_{ij}^C , the dissipative force \mathbf{F}_{ij}^D , and the random force \mathbf{F}_{ij}^R are given by⁴⁴:

$$\begin{aligned} \mathbf{F}_{ij}^C &= a_{ij} \omega_C(r_{ij}) \mathbf{e}_{ij}, \\ \mathbf{F}_{ij}^D &= -\gamma_{ij} \omega_D(r_{ij}) (\mathbf{e}_{ij} \cdot \mathbf{v}_{ij}) \mathbf{e}_{ij}, \\ \mathbf{F}_{ij}^R &= \sigma_{ij} \omega_R(r_{ij}) \xi_{ij} \Delta t^{-1/2} \mathbf{e}_{ij}. \end{aligned}$$

Here, $r_{ij} = |\mathbf{r}_{ij}|$ is the distance between the beads i and j , \mathbf{e}_{ij} the unit vector in the direction of \mathbf{r}_{ij} , \mathbf{v}_{ij} is the relative velocity of the bead i with respect to the bead j and Δt is the time step. a_{ij} is a repulsive force parameter. For similar beads, a_{ii} can be determined by matching the compressibility of the fluid using the following⁷⁵:

$$a_{ii} = k_B T (\kappa_c^{-1} N_m - 1.0) / 2\alpha\rho, \quad (\text{B1})$$

where $\alpha = 0.101 \pm 0.001$ for liquid water which arises from the DPD equation of state⁴⁴. κ_c^{-1} is the dimensionless compressibility of the fluid, given by⁴⁴

$$\kappa_c^{-1} = \frac{1}{\rho k_B T \kappa_T}, \quad (\text{B2})$$

where ρ is the number density of the molecules and κ_T is the isothermal compressibility of the fluid. For beads of different types, the values of a_{ij} are determined to reproduce the mutual solubility of different species by matching the Flory-Huggins χ -parameters⁴⁴. $\xi_{ij}(t)$ is a randomly fluctuating variable with Gaussian statistics, such that $\langle \xi_{ij}(t) \rangle = 0$, $\text{Var}(\xi_{ij}) = 1$, and $\langle \xi_{ij}(t) \xi_{kl}(t') \rangle = (\delta_{ik} \delta_{jl} + \delta_{il} \delta_{jk}) \delta(t - t')$. The dissipative force and the random force jointly act as a thermostat provided that the dissipative parameter γ_{ij} and the amplitude of the noise σ_{ij} satisfy the fluctuation-dissipation equilibrium, which requires $\sigma_{ij}^2 = 4\gamma_{ij} k_B T$ and $\omega_D(r_{ij}) = \omega_R^2(r_{ij})$. A common choice for the weight functions is $\omega_C(r_{ij}) = 1 - r_{ij}/r_c$ and $\omega_D(r_{ij}) = (1 - r_{ij}/r_c)^s$ for $r \leq r_c$ and zero for $r > r_c$, where r_c is the cutoff radius. The exponent s can be modified

to adjust the kinematic viscosity and diffusivity of the liquid, thereby achieving a desired Schmidt number⁷⁶. It is common to use $s = 2$ following the original DPD formulation, but in this work, we consider $s = 0.5$ which allows to reach $Sc \approx 10$ (instead of $Sc \approx 1$ for $s = 2$)⁷⁶.

Additional bond interactions are necessary to link lipid chain beads. A commonly used approach is applying translational (U_T) and angular (U_θ) harmonic spring potentials, as follows:

$$\begin{aligned} U_T &= \frac{1}{2} k_T (r - r_{eq})^2, \\ U_\theta &= \frac{1}{2} k_\theta (\theta - \theta_{eq})^2. \end{aligned}$$

Here, r_{eq} and θ_{eq} denote the equilibrium bond length and angle, respectively, while k_T and k_θ represent the spring constant and angular bending stiffness.

Appendix C: DPD Parameters

The isothermal compressibility of water at atmospheric pressure and reference temperature $T = 300 \text{ K}$ is $\kappa_T = 4.5 \times 10^{-10} \text{ Pa}^{-1}$ (see Ref. [77]). Using Eq. (B2), we calculate $\kappa_c^{-1} = 16.01 [k_B T / \ell_0^3]$. Consequently, from Eq. (B1), we determine the interaction coefficient $a_{ww} = 78$ for the water beads. The a_{ij} , parameters for the other species are adopted from Groot and Rabon⁷⁸ and summarized in Table II.

TABLE II. Repulsive a_{ij} interaction parameter between the species.

| bead type | w | c | e | t |
|-----------|------|------|------|------|
| w | 78 | 104 | 79.3 | 79.3 |
| c | 104 | 78 | 86.7 | 104 |
| e | 79.3 | 86.7 | 78 | 79.3 |
| h | 75.8 | 104 | 79.3 | 86.7 |

The dissipative parameter $\gamma_{ij} = 4.5$ and the exponent $s = 0.5$ are used for all bead interactions. The cut-off radius $r_c = 1$ is used for all species and interactions.

For the bonded beads, the linear spring constant is $k_T = 4.0$, and the equilibrium bond length is $r_{eq} = 0$. The bending stiffness is $k_\theta = 6.0$, with equilibrium bond angles $\theta_1 = 180^\circ$, $\theta_2 = 90^\circ$, and $\theta_3 = 135^\circ$.

Appendix D: Bulk Fluid Properties

Here, we characterize the dynamic and structural properties of the solvent molecules (\mathbf{z} type beads) in the bulk.

a. Self-diffusion coefficient. The self-diffusivity of the fluid D_b is determined in the absence of an interface, from the mean-squared displacement of the DPD beads, which is displayed in Fig. 12(a) as a function of time. After an initial ballistic regime, motion is diffusive ($\text{MSD} \propto t$) for $t \gtrsim 0.1 \tau_0$. The slope of the line in the diffusive regime represents the self-diffusivity of the fluid, which we can quantify to be $D_b = 0.092 \ell_0^2 / \tau_0$.

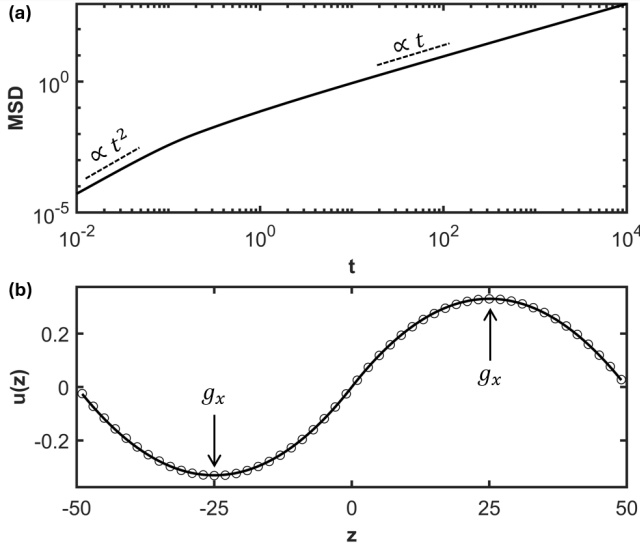


FIG. 12. (a) Time evolution of the mean-squared displacement (divided by 6) of the solvent molecules. The time and MSD are indicated in τ_0 and ℓ_0^2 unit, respectively. (b) Velocity profile obtained from the Poiseuille flow simulation (circles). The coordinate z and the velocity are indicated in ℓ_0 and ℓ_0/τ_0 units, respectively. The line is a fit using Eq. (D1). The computational domain here is $(L_x \times L_y \times L_z) = (10 \times 100 \times 100)\ell_0^3$.

b. Viscosity. The kinematic viscosity is determined using a periodic Poiseuille flow method⁷⁹ by fitting the analytical solution

$$u(z) = g_x z(d - |z|)/2\nu \quad (\text{D1})$$

to the velocity profile obtained from sheared DPD simulations. Here, ν is the kinematic viscosity, $g_x = 0.001\ell_0/\tau_0^2$ is the body force per unit mass applied to each DPD bead, and $d = 50\ell_0$ is half the length of the computational domain in the z -direction. The velocity profile obtained from the DPD simulation and the fitted analytical solution are shown in Fig. 12(b). We find $\nu = 0.94 \ell_0^2/\tau_0$.

c. Pair distribution function. Another quantity of interest is the characteristic distance between the DPD molecules. The unique length scale prescribed in the DPD method is the cut-off distance of the pairwise forces, which here we take to be the same for all force contributions: conservative, dissipative and random. This length scale is not necessarily representative of the distance between molecules. Instead, we find the characteristic distance between the DPD molecules (or points) from the distance at which the largest peak of the radial pair distribution function occurs, here $0.82 \ell_0$ – see Fig. 13. Thus, we determine a characteristic bead "radius" equal to half this distance, *i.e.* $a = 0.41 \ell_0$.

Appendix E: Diffusive solvent dynamics near flat and undulated rigid membranes

In Figs. 14 and 15 we report the standard deviation of solvent motion in the different slabs near the flat and undulated rigid

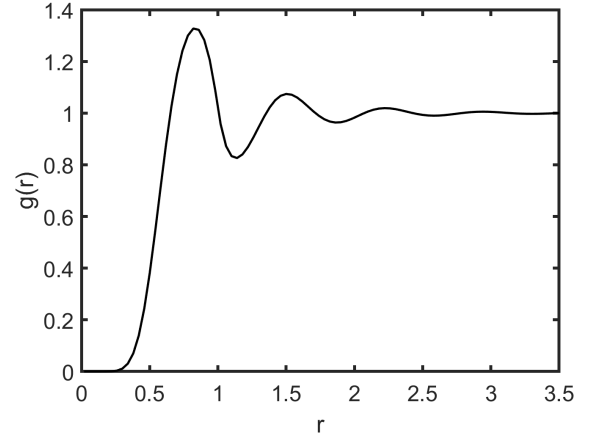


FIG. 13. Radial pair distribution function of the solvent molecules. The distance r is indicated in ℓ_0 unit.

membranes respectively, with the fluctuating membrane case superimposed for comparison.

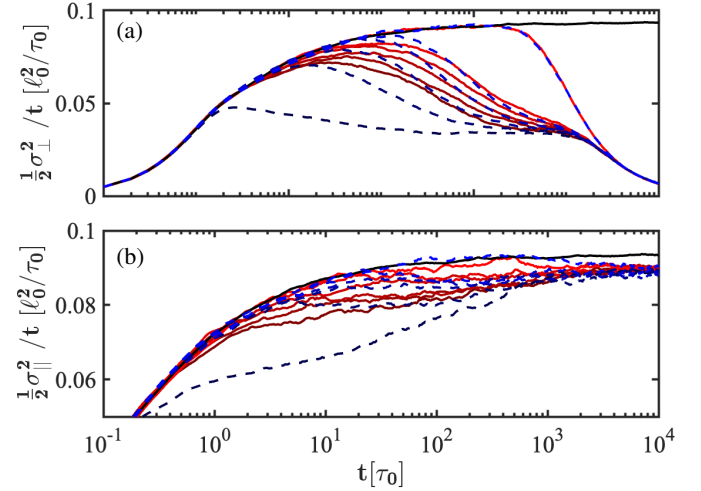


FIG. 14. Comparison of the time evolution of $\frac{1}{2} \frac{\sigma_{\perp,\parallel}^2(t)}{t}$ in the (a) perpendicular and (b) parallel directions, between simulations with a fluctuating membrane (red) and a rigid wall (dashed blue). Red or blue lines, from darkest to lightest, represent slabs at distances of 0.5, 1.5, 2.5, 3.5, 4.5 and $19.5 \ell_0$ from the fluctuating membrane surface. Black lines indicate the bulk case.

Appendix F: Vertical displacements of solvent molecules

We investigate here the probability distribution functions (PDF) of molecular displacement $P(\delta z)$. Fig. 16a shows the PDF of vertical displacements at time $t = \tau_0$ which roughly corresponds to the end of the ballistic regime. At this early time, the PDF curves remain symmetric (Gaussian) at different distances from the different interfaces, except very close to the flat wall. There, we notice a slight asymmetry in the PDF, towards positive (upward) displacements. This is due to

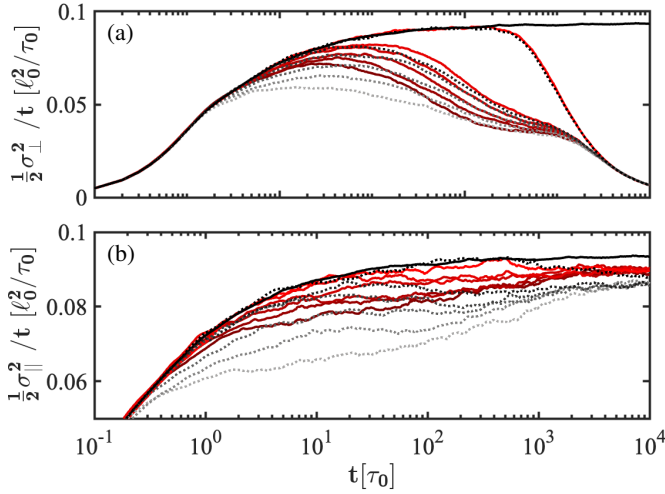


FIG. 15. Comparison of the time evolution of $\frac{1}{2} \frac{\sigma_{\perp}^2(t)}{t}$ in the (a) perpendicular and (b) parallel directions, between simulations with a fluctuating membrane (red) and a rigid membrane (dotted gray). Red or blue lines, from darkest to lightest, represent slabs at distances of 0.5, 1.5, 2.5, 3.5, 4.5 and $19.5 \ell_0$ from the fluctuating membrane surface. Black lines indicate the bulk case.

the repulsion of molecules by the rigid flat wall.

Fig. 16b shows the PDF of vertical displacements at time $t = 10 \tau_0$ which corresponds roughly to the molecular diffusion time scale. We recall that $t = 10 \tau_0$ also corresponds to the time it takes for the solvent molecules to diffuse along a distance equal to the slab height ℓ_0 . The asymmetry of the PDF between negative displacements (toward the interface) and positive displacements (away from the interface) is apparent for different layers and on different interfaces. Clearly, in the rigid flat wall case, repulsion is felt quite strongly on 3 layers above the wall. In contrast, in both rigid and fluctuating membrane cases, there is only a mild repulsion by the walls, and mostly on the 2 first layers. This corroborates the hypothesis that the wavy nature of the interface traps molecules near the interface.

Note that the PDF of the longitudinal displacements (not shown here) remained symmetric and did not show significant time dependence, regardless of the nature of the interface and the distance to it.

Appendix G: Membrane dynamics

The intensity of membrane height fluctuations, as well as the rate of their relaxation in time depend on the wavenumber. Several post-processing steps are required to characterize the membrane relaxation time scales. First, the lipid beads in the membrane are distributed on a 32×32 two-dimensional grid (parallel to the membrane). Second, the membrane height $h(\mathbf{x}, t)$ on each grid point \mathbf{x} is given by the average of the z coordinates of the beads in that grid point. $z = 0$ is set at the time-averaged position of the membrane midplane. Third, the power spectrum $\langle |h_q^2(t)| \rangle$ of the height fluctuation of each

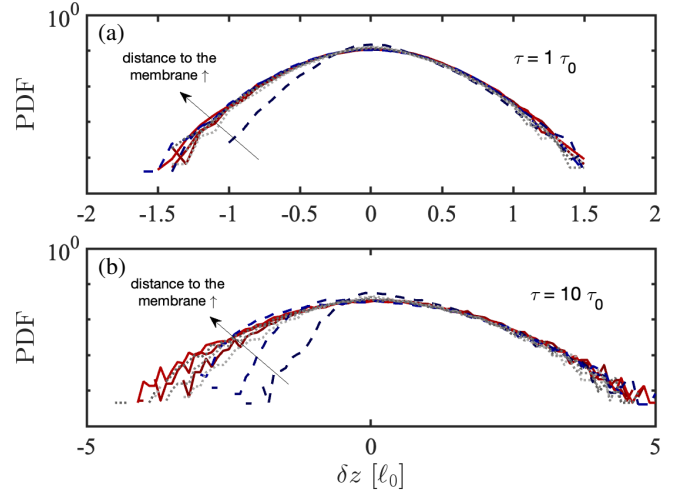


FIG. 16. Normalized probability density function $P(\delta z)$ of vertical bead displacements δz at different time points (a) $t = \tau_0$ and (b) $t = 10 \tau_0$, at different distances from the different interfaces: fluctuating membrane (red), flat wall (blue) and rigid membrane (gray). Dark to light colors represent slabs at distances 0.5, 1.5, and $2.5 \ell_0$ with respect to the membrane surface.

undulating mode with wavenumber q is calculated. Here $\langle \cdot \rangle$ is an average over time only. Fourth, the time autocorrelation function of the height fluctuations is computed, $F(q, t) = \langle |h_q|(t) |h_q|(0) \rangle$. The decay in time of the autocorrelation function for different q is shown in Fig. 8a.

When integrating $F(q, t)$ to calculate the relaxation time $\tau_r(q)$ from Eq. (6), we set a cutoff value on t , such that $F(q, t)/F(q, 0) > 0.05$ to avoid integrating noise. A smaller cutoff of 0.1 has no significant influence on the calculated relaxation time.

Appendix H: Force balance on the solvent slabs

A force balance in the z direction (normal to the membrane), originating from an overdamped Langevin equation for particle motion, can be written as follows:

$$F_{\text{eq}}(z) + F_{\text{drag}}(z) + F_{\text{mn}}(z) + F_{\text{int}}(z) = 0, \quad (\text{H1})$$

where the term

$$F_{\text{eq}}(z) = \frac{dU_{\text{eq}}}{dz}$$

results from equilibrium interactions with the membrane through an interaction potential $U_{\text{eq}}(z)$. It can be inferred from the density profile of the solvent molecules at equilibrium, which obeys Boltzmann distribution and so $U_{\text{eq}}(z) = -k_B T \ln(\rho(z)/\rho)$.

The second term $F_{\text{drag}}(z)$ corresponds to the Stokes drag experienced by the solvent molecules while they drift away from the interface. The drag force can be modeled using the drift

velocity of the solvent molecules and considering that the bead mobility is reduced near the interface

$$F_{\text{drag}}(z) = -\gamma(z)v_{\perp} \equiv -\frac{k_B T}{D_{\perp}(z)}v_{\perp},$$

where $\gamma(z) = k_B T / D_{\perp}(z)$ is the friction coefficient, and v_{\perp} is the velocity of the molecules perpendicular to the interface. This velocity was estimated from a time average between $t = 0$ and $t = 10 \tau_0$ of the instantaneous velocity $\frac{\langle \delta z(t + \delta t) \rangle - \langle \delta z(t) \rangle}{\delta t}$ with $\delta t = 0.1 \tau_0$.

The third term $F_{\text{mn}}(z)$ corresponds to multiplicative noise or spurious drift

$$F_{\text{mn}}(z) = \frac{k_B T}{D_{\perp}(z)} \frac{dD_{\perp}}{dz}$$

and arises from the coupling between the random motion and the dependence of molecule mobility on the distance to the interface. Like the classic drag, this contribution is a resisting force. We can understand it as a resistance against the collective diffusion of the molecules from regions of larger diffusion toward regions of lower diffusion. The derivative of the diffusion coefficient was calculated as $\frac{dD_{\perp}}{dz} = \frac{D_{\perp,i+1} - D_{\perp,i}}{z_{i+1} - z_i}$, where i refers to the slab index and z_i is the position of the center of the slab.

The last term $F_{\text{int}}(z)$ denotes a force that may result from the interaction between the freely moving particles and the interface, either due to electrostatic forces if present or due to elastic effects associated with membrane fluctuations in the present study.

Our simulations allow us to measure numerically three contributions to the force experienced by the solvent molecules, $F_{\text{eq}}(z)$, $F_{\text{drag}}(z)$ and $F_{\text{mn}}(z)$ and compare them. Fig. 17a shows, in blue, v_{\perp} , the drift velocity of the solvent molecules as a function of the distance to the interface. The drift is stronger near the flat wall compared to the membrane cases, in agreement with the observations made on particle displacements in Sec. IV A. The decay of v_{\perp} occurs at short length scales, typically around $3 - 4 \ell_0$, which is comparable to the maximum height fluctuations (displayed in Fig. 2). Fig. 17b displays the spurious drift velocity associated with the gradient of the molecules' mobility dD_{\perp}/dz . The amplitude of this spurious drift is smaller than the amplitude of the average drift, perpendicularly to the interface. Strikingly, both membranes exhibit only a very weak contribution to spurious drift, due to the nearly flat diffusive profile $D_{\perp}(z)$ (see Fig. 6a), in agreement with the “smoothing” effect associated with averaging along each membrane's surface over wells and bumps.

Now we can examine the different terms in the force balance. F_{drag} and F_{mn} are of the same nature, *i.e.* they are both written in the form of a product of a molecule's mobility and

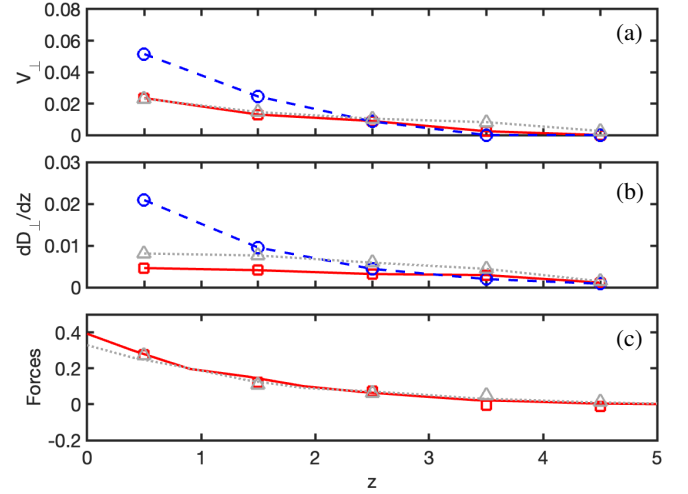


FIG. 17. a) Average drift velocity, b) derivative of the normal diffusion coefficient and c) forces experienced by the solvent molecules as a function of the distance to the interface. In a) and b), red squares, blue circles and gray triangles are obtained from simulations with a fluctuating membrane, a flat wall and a rigid membrane, respectively, while the lines are used for eye guidance. In c), red squares and gray triangles correspond to $-(F_{\text{drag}} + F_{\text{mn}})$ whereas red solid and gray dotted lines correspond to F_{eq} , obtained from simulations with a fluctuating (red) and a rigid membrane (gray). The coordinate z and the forces are indicated in ℓ_0 and $\sqrt{k_B T}/\ell_0$ units respectively, whereas the derivative of the diffusion coefficient and the drift velocity are indicated in ℓ_0/τ_0 units.

a relative velocity. However, they apply in opposite directions: the first points towards the membrane unlike the second which points away from it. We lump them in a single term which corresponds to the effective drag. Their negative sum $-(F_{\text{drag}} + F_{\text{mn}}) = k_B T / D_{\perp}(z)(v_{\perp} - dD_{\perp}(z)/dz)$ is shown in Fig. 17c, using symbols. The continuous lines correspond to F_{eq} , using the density profiles displayed in Fig. 3. Fig. 17c clearly shows that the effective drag and the equilibrium force are well balanced, for both the fluctuating and rigid membrane cases. Note that similar conclusions can be made in the case of a flat wall (not shown here), with the difference that F_{eq} is not a smooth function in that case, due to the sharp decay of the equilibrium bead distribution. We conclude that non-conservative or elastic forces are absent, at least during the diffusive time range.

¹T. Nguyen, B. R. J. Narayanareddy, S. P. Gross, and C. E. Miles, PLOS Computational Biology **20**, e1012158 (2024).

²M. A. Lomholt, I. M. Zaid, and R. Metzler, Physical review letters **98**, 200603 (2007).

³E. Kätelhön, S. V. Sokolov, and R. G. Compton, Sensors and Actuators B: Chemical **234**, 420 (2016).

⁴N. Kaiser, Applied optics **41**, 3053 (2002).

⁵G. G. Stokes *et al.*, (1851).

⁶H. A. Lorentz, Hendrik Antoon Lorentz: Abhandlungen über theoretische Physik. Leipzig: Teubner **1**, 43 (1907).

⁷S. Wakiya, Res. Rep. Fac. Eng. Niigata Univ. (1960).

⁸H. Faxén, *Einwirkung der Gefäßwände auf den Widerstand gegen die Bewegung einer kleinen Kugel in einer zähen Flüssigkeit* (Förf., 1921).

⁹C. W. Oseen, *Neuere methoden und ergebnisse in der hydrodynamik*, Vol. 1 (Akademische Verlagsgesellschaft, 1927).

- ¹⁰X. Bian, C. Kim, and G. E. Karniadakis, *Soft Matter* **12**, 6331 (2016).
- ¹¹H. Brenner, *Chemical Engineering Science* **16**, 242 (1961).
- ¹²E. Honig, G. Roeberson, and P. Wiersema, *Journal of Colloid and Interface Science* **36**, 97 (1971).
- ¹³M. A. Bevan and D. C. Prieve, *The Journal of Chemical Physics* **113**, 1228 (2000).
- ¹⁴A. J. Goldman, R. G. Cox, and H. Brenner, *Chemical engineering science* **22**, 637 (1967).
- ¹⁵M. O'Neill and K. Stewartson, *Journal of Fluid Mechanics* **27**, 705 (1967).
- ¹⁶G. Perkins and R. Jones, *Physica A: Statistical Mechanics and its Applications* **189**, 447 (1992).
- ¹⁷M. D. Carbajal-Tinoco, R. Lopez-Fernandez, and J. L. Arauz-Lara, *Physical review letters* **99**, 138303 (2007).
- ¹⁸F. Quemeneur, J. K. Sigurdsson, M. Renner, P. J. Atzberger, P. Bassereau, and D. Lacoste, *Proceedings of the National Academy of Sciences* **111**, 5083 (2014).
- ¹⁹P. Girard, J. Prost, and P. Bassereau, *Physical review letters* **94**, 088102 (2005).
- ²⁰E. G. Brandt, A. R. Braun, J. N. Sachs, J. F. Nagle, and O. Edholm, *Biophysical journal* **100**, 2104 (2011).
- ²¹S. Marbach, D. S. Dean, and L. Bocquet, *Nature Physics* **14**, 1108 (2018).
- ²²Y. Wang, D. S. Dean, S. Marbach, and R. Zakine, *Journal of Fluid Mechanics* **972**, A8 (2023).
- ²³S. Marbach and K. Alim, *Physical Review Fluids* **4**, 114202 (2019).
- ²⁴R. Sarfati, C. P. Calderon, and D. K. Schwartz, *ACS nano* **15**, 7392 (2021).
- ²⁵B. Chakrabarti and D. Saintilan, *Physics of Fluids* **32**, 113102 (2020).
- ²⁶G. I. Taylor, *Proceedings of the Royal Society of London. Series A. Mathematical and Physical Sciences* **219**, 186 (1953), <https://royalsocietypublishing.org/doi/pdf/10.1098/rspa.1953.0139>.
- ²⁷R. Aris, *Proceedings of the Royal Society of London. Series A. Mathematical and Physical Sciences* **235**, 67 (1956).
- ²⁸S. Sheikh, B. Lonetti, I. Touche, A. Mohammadi, Z. Li, and M. Abbas, *J. Chem. Phys.* **159** (2023).
- ²⁹N. Kavokine, R. R. Netz, and L. Bocquet, *Annual Review of Fluid Mechanics* **53**, 377 (2021).
- ³⁰D. Camargo, J. De La Torre, D. Duque-Zumajo, P. Español, R. Delgado-Buscalioni, and F. Chejne, *J. Chem. Phys.* **148** (2018).
- ³¹F. Leroy, B. Rousseau, and A. Fuchs, *Physical Chemistry Chemical Physics* **6**, 775 (2004).
- ³²E. Haldoupis, T. Watanabe, S. Nair, and D. S. Sholl, *ChemPhysChem* **13**, 3449 (2012).
- ³³N. Fares, M. Lavaud, Z. Zhang, A. Jha, Y. Amarouchene, and T. Salez, *arXiv preprint arXiv:2405.13434* (2024).
- ³⁴M. Ma, F. Grey, L. Shen, M. Urbakh, S. Wu, J. Z. Liu, Y. Liu, and Q. Zheng, *Nature nanotechnology* **10**, 692 (2015).
- ³⁵M. Ma, G. Tocci, A. Michaelides, and G. Aeppli, *Nature materials* **15**, 66 (2016).
- ³⁶W. Cao, J. Wang, and M. Ma, *The Journal of Physical Chemistry Letters* **10**, 7251 (2019).
- ³⁷Y. Noh and N. Aluru, *Nano letters* **22**, 419 (2021).
- ³⁸H. Yoshida, V. Kaiser, B. Rotenberg, and L. Bocquet, *Nature communications* **9**, 1 (2018).
- ³⁹F. Sedlmeier, Y. von Hansen, L. Mengyu, D. Horinek, and R. R. Netz, *J. Stat. Phys.* **145**, 240 (2011).
- ⁴⁰Y. von Hansen, S. Gekle, and R. R. Netz, *Physical review letters* **111**, 118103 (2013).
- ⁴¹Z. Li, X. Bian, B. Caswell, and G. E. Karniadakis, *Soft Matter* **10**, 8659 (2014).
- ⁴²A. Gubbiotti, M. Baldelli, G. Di Muccio, P. Magaretti, S. Marbach, and M. Chinappi, *Advances in Physics: X* **7**, 2036638 (2022).
- ⁴³M. Kranenburg, J.-P. Nicolas, and B. Smit, *Phys. Chem. Chem. Phys.* **6**, 4142 (2004).
- ⁴⁴R. D. Groot and P. B. Warren, *The Journal of chemical physics* **107**, 4423 (1997).
- ⁴⁵P. Espanol and P. Warren, *Europhysics letters* **30**, 191 (1995).
- ⁴⁶A. P. Thompson, H. M. Aktulga, R. Berger, D. S. Bolintineanu, W. M. Brown, P. S. Crozier, P. J. in 't Veld, A. Kohlmeyer, S. G. Moore, T. D. Nguyen, R. Shan, M. J. Stevens, J. Tranchida, C. Trott, and S. J. Plimpton, *Comp. Phys. Comm.* **271**, 108171 (2022).
- ⁴⁷A. Vilquin, V. Bertin, P. Soulard, G. Guyard, E. Raphaël, F. Restagno, T. Salez, and J. D. McGraw, *Phys. Rev. Fluids* **6**, 064201 (2021).
- ⁴⁸W. Pan, D. A. Fedosov, G. E. Karniadakis, and B. Caswell, *Phys. Rev. E* **78**, 046706 (2008).
- ⁴⁹W. E. Alley and B. J. Alder, *Physical Review A* **27**, 3158 (1983).
- ⁵⁰F. Balboa Usabiaga, X. Xie, R. Delgado-Buscalioni, and A. Donev, *The Journal of chemical physics* **139** (2013).
- ⁵¹M. Vergeles, P. Keblinski, J. Koplik, and J. R. Banavar, *Physical Review E* **53**, 4852 (1996).
- ⁵²L. Bocquet, J.-P. Hansen, and J. Piasecki, *Journal of statistical physics* **76**, 527 (1994).
- ⁵³B. Alder, W. Alley, and E. Pollock, *Berichte der Bunsengesellschaft für physikalische Chemie* **85**, 944 (1981).
- ⁵⁴S. Lee, R. Chadwick, and L. Leal, *J. Fluid Mech.* **93**, 705 (1979).
- ⁵⁵E. Olsén, S. Jöemetsa, A. González, P. Joyce, V. P. Zhdanov, D. Midtvedt, and F. Hook, *Nano letters* **21**, 8503 (2021).
- ⁵⁶E. Lauga and T. M. Squires, *Phys. Fluids* **17** (2005).
- ⁵⁷E. Lauga, M. Brenner, and H. Stone, in *Springer Handbooks* (Springer, 2007) pp. 1219–1240.
- ⁵⁸E. Secchi, S. Marbach, A. Niguès, D. Stein, A. Siria, and L. Bocquet, *Nature* **537**, 210 (2016).
- ⁵⁹A. Daddi-Moussa-Ider, A. Guckenberger, and S. Gekle, *Physical Review E* **93**, 012612 (2016).
- ⁶⁰R. Zwanzig, *The Journal of Physical Chemistry* **96**, 3926 (1992).
- ⁶¹M. H. Jacobs, (Springer Berlin Heidelberg, Berlin, Heidelberg, 1967).
- ⁶²D. Reguera and J. M. Rubí, *Physical Review E* **64**, 061106 (2001).
- ⁶³P. Kalinay and J. K. Percus, *Physical Review E* **74**, 041203 (2006).
- ⁶⁴J. M. Rubi, *EPL (Europhysics Letters)* **127**, 10001 (2019).
- ⁶⁵E. G. Brandt and O. Edholm, *The Journal of chemical physics* **133** (2010).
- ⁶⁶U. Seifert and S. Langer, *Europhys. Lett.* **23**, 71 (1993).
- ⁶⁷S. Shkulipa, W. den Otter, and W. Briels, *J. Chem. Phys.* **125** (2006).
- ⁶⁸R. Groot and K. Rabone, *Biophysical J.* **81**, 725 (2001).
- ⁶⁹A. Schlaich, M. Vandamme, M. Plazanet, and B. Coasne, *ACS nano* (2024).
- ⁷⁰B. Coquinot, L. Bocquet, and N. Kavokine, *Physical Review X* **13**, 011019 (2023).
- ⁷¹M. Lizée, A. Marcotte, B. Coquinot, N. Kavokine, K. Sobnath, C. Barraud, A. Bhardwaj, B. Radha, A. Niguès, L. Bocquet, *et al.*, *Physical Review X* **13**, 011020 (2023).
- ⁷²F. Detcheverry and L. Bocquet, *Phys. Rev. E* **88**, 012106 (2013).
- ⁷³L. Bocquet and J.-L. Barrat, *The Journal of chemical physics* **139** (2013).
- ⁷⁴J. Lu, Z. Li, R. Thomas, E. Staples, I. Tucker, and J. Penfold, *The Journal of Physical Chemistry* **97**, 8012 (1993).
- ⁷⁵I. V. Pivkin, B. Caswell, and G. E. Karniadakis, *Reviews in computational chemistry* **27**, 85 (2010).
- ⁷⁶Z. Li, Y.-H. Tang, H. Lei, B. Caswell, and G. E. Karniadakis, *Journal of Computational Physics* **265**, 113 (2014).
- ⁷⁷G. S. Kell, *Journal of Chemical and Engineering Data* **15**, 119 (1970).
- ⁷⁸R. D. Groot and K. Rabone, *Biophysical journal* **81**, 725 (2001).
- ⁷⁹J. Backer, C. Lowe, H. Hoefsloot, and P. Iedema, *The Journal of chemical physics* **122** (2005).